

# BigReg: An Efficient Registration Pipeline for High-Resolution X-Ray and Light-Sheet Fluorescence Microscopy

Siyuan Mei <sup>1</sup>, Fuxin Fan <sup>1</sup>, Mareike Thies <sup>1</sup>, Mingxuan Gu <sup>1</sup>, Fabian Wagner <sup>1</sup>, Oliver Aust <sup>2</sup>, Ina Erceg <sup>3</sup>, Zeynab Mirzaei <sup>4</sup>, Georgiana Neag <sup>2</sup>, Yipeng Sun <sup>1</sup>, Yixing Huang <sup>5</sup>, Andreas Maier <sup>1</sup>,

<sup>1</sup> Pattern Recognition Lab, Friedrich-Alexander University Erlangen-Nuremberg, Erlangen, Germany

<sup>2</sup> Department of Internal Medicine 3 - Rheumatology and Immunology, University Hospital Erlangen, Erlangen, Germany

<sup>3</sup> Fraunhofer Institute for Ceramic Technologies and Systems - IKTS, Forcheim, Germany

<sup>4</sup> Institute for Nanotechnology and Correlative Microscopy - INAM GmbH, Forcheim, Germany

<sup>5</sup> Institute of Medical Technology, Peking University, Beijing, China

## Abstract

Recently, X-ray microscopy (XRM) and light-sheet fluorescence microscopy (LSFM) have emerged as pivotal tools in preclinical research, particularly for studying bone remodeling diseases such as osteoporosis. These modalities offer micrometer-level resolution, and their integration allows for a complementary examination of bone microstructures which is essential for analyzing functional changes. However, registering high-resolution volumes from these independently scanned modalities poses substantial challenges, especially in real-world and reference-free scenarios. This paper presents BigReg, a fast, two-stage pipeline designed for large-volume registration of XRM and LSFM data. The first stage involves extracting surface features and applying two successive point cloud-based methods for coarse alignment. The subsequent stage refines this alignment using a modified cross-correlation technique, achieving precise volumetric registration. Evaluations using expert-annotated landmarks and augmented test data demonstrate that BigReg approaches the accuracy of landmark-based registration with a landmark distance (LMD) of  $8.36 \mu\text{m} \pm 0.12 \mu\text{m}$  and a landmark fitness (LM fitness) of  $85.71\% \pm 1.02\%$ . Moreover, BigReg can provide an optimal initialization for mutual information-based methods which otherwise fail independently, further reducing LMD to  $7.24 \mu\text{m} \pm 0.11 \mu\text{m}$  and increasing LM fitness to  $93.90\% \pm 0.77\%$ . Ultimately, key microstructures, notably lacunae in XRM and bone cells in LSFM, are accurately aligned, enabling unprecedented insights into the pathology of osteoporosis.

## Keywords

Microscopy Image Registration, Multi-Modality, High-Resolution Volume

## Article informations

Corresponding author: siyuan.mei@fau.de

©YYYYY Name1 and Name2. License: CC-BY 4.0

## 1. Introduction

**O**steoporosis (OP) is the predominant cause of fragility fractures among the elderly, characterized by age-related bone loss and deterioration of the bone microarchitecture (Clynes et al., 2020). The latest systematic review reported a global osteoporosis prevalence of 19.7%, with postmenopausal women exhibiting the highest rate at 27.4% (Xiao et al., 2022). Pathologically, this disease arises from imbalanced bone remodeling governed by various bone cells, such as osteocytes (Raggatt and Partridge, 2010). These osteocytes reside within microscopic cavities called lacunae, which are a few micrometers in size and interconnected through tiny canals (Buenzli and Sims, 2015; Peyrin et al., 2014). In preclinical studies, ovariec-

tomized rodent (OVX) models, established by removing the ovaries from female mice or rats, are commonly used to mimic the estrogen deficiency-induced bone loss seen in postmenopausal women (Yousefzadeh et al., 2020). Conventional biological investigations monitor trabecular bone density in OVX models using micro-computed tomography (CT) (Xiong et al., 2021; Akhter and Recker, 2021). However, two significant limitations of micro-CT prevent deep exploration into the mechanisms behind micro-architectural deterioration at the cellular scale: the resolution around 20-50  $\mu\text{m}$  is insufficient to resolve the lacunae (Thies et al., 2022; Longo et al., 2017), and its monomodality cannot capture the interaction between the lacunae and the osteocytes they host. To address these shortcomings, recent research has utilized X-ray microscopy (XRM) (Langer

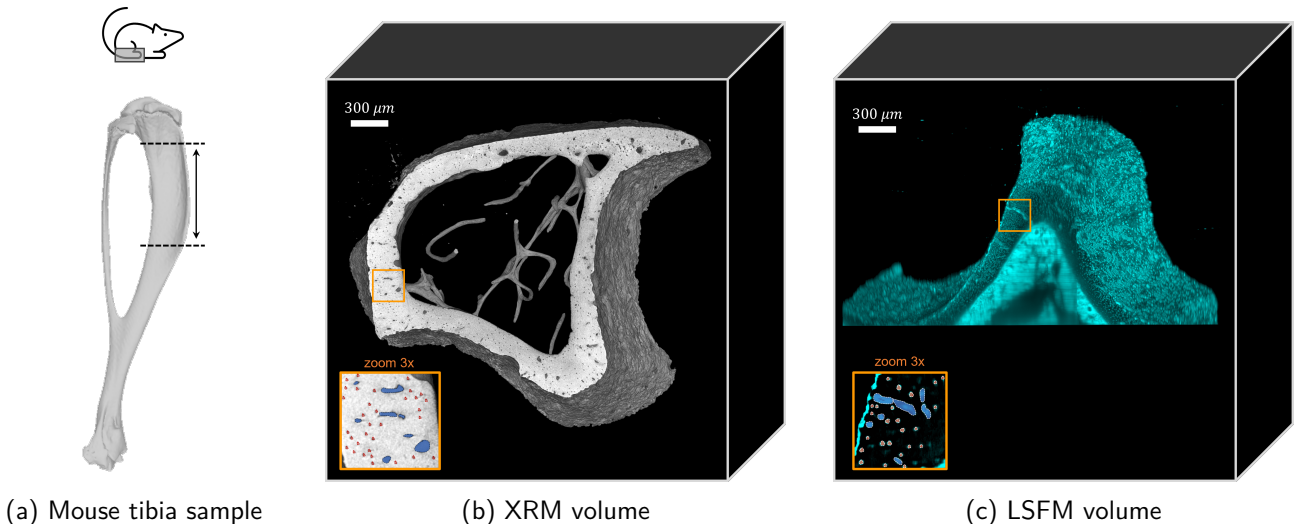


Figure 1: Visualization of (a) a mouse tibia sample used as the scanning subject and 3D rendered volume for (b) XRM data and (c) LSFM data. Both volumes are grayscale but shown in different colors, and their voxel sizes and shapes are unified to  $1.42 \times 1.42 \times 1.42 \mu\text{m}^3$  and  $2048 \times 2048 \times 800$ , respectively. While the XRM scan reconstructs the complete bone structure, the LSFM scan omits the lower part of the bone cross-section due to increased scattering along the detection depth. In the highlighted subregions within the orange boxes, which are magnified threefold, the XRM volume features vessel canals (blue labels) and lacunae (red labels), whereas the LSFM volume shows vessels (blue labels) and cell nuclei (red labels).

and Peyrin, 2016) and light-sheet fluorescence microscopy (LSFM) (Thai et al., 2024; Xiao et al., 2024) to generate volumetric data from mouse bones at single-micrometer precision. These advanced modalities provide complementary 3D views, with XRM revealing detailed bone morphology and LSFM highlighting cellular and vascular structures within the bones (see details in Fig. 1). Early efforts combining these modalities supported by expert observation have unveiled the significance of small transcortical vessels (Grüneboom et al., 2019). Nonetheless, this manual approach is not only laborious but also falls short for finer structures which are essential for innovative osteoporosis metrics, such as the ratio of empty lacunae to those containing bone cells. To advance this research and fully exploit the potential of these scans, the development of an automated algorithm for precise registration of XRM and LSFM volumes has become a priority.

In this paper, we propose BigReg, a highly efficient two-stage registration pipeline for high-resolution XRM and LSFM volumes, as depicted in Fig. 2. Given a volume pair as input, the first stage extracts surface points and then performs a global-to-local point cloud registration, providing a coarse alignment. Crucially, this initial alignment is refined in the second stage through an efficient search for the remaining transformation in the Fourier domain based on a modified cross-correlation method. Our results suggest that BigReg can match the performance of manual landmark-based methods and is robust against significant

misregistrations. The main contributions are summarized as follows:

- This is the first work that successfully performs automatic registration between high-resolution XRM and LSFM volumes while attaining micrometer-scale accuracy.
- The combination of point cloud-based and cross-correlation methods considers both surface features and full image contents, achieving coarse to fine registration within two stages.
- The entire pipeline is both memory- and computation-efficient, achieved by minimizing the data amount through surface feature extraction in the first stage and reducing computational load via Fourier transformation in the second stage.
- Last but not least, we elucidate the critical role of the initial transformation in MI-based methods and demonstrate how BigReg can serve as an optimal initializer, thus enhancing the quest for ultimate registration precision

## 2. Related Works

Image registration refers to aligning one image (the moving image) with another image (the fixed image) by identifying the appropriate spatial transform. This field has undergone significant exploration over the past four decades, particularly in different medical imaging modalities (Saiti

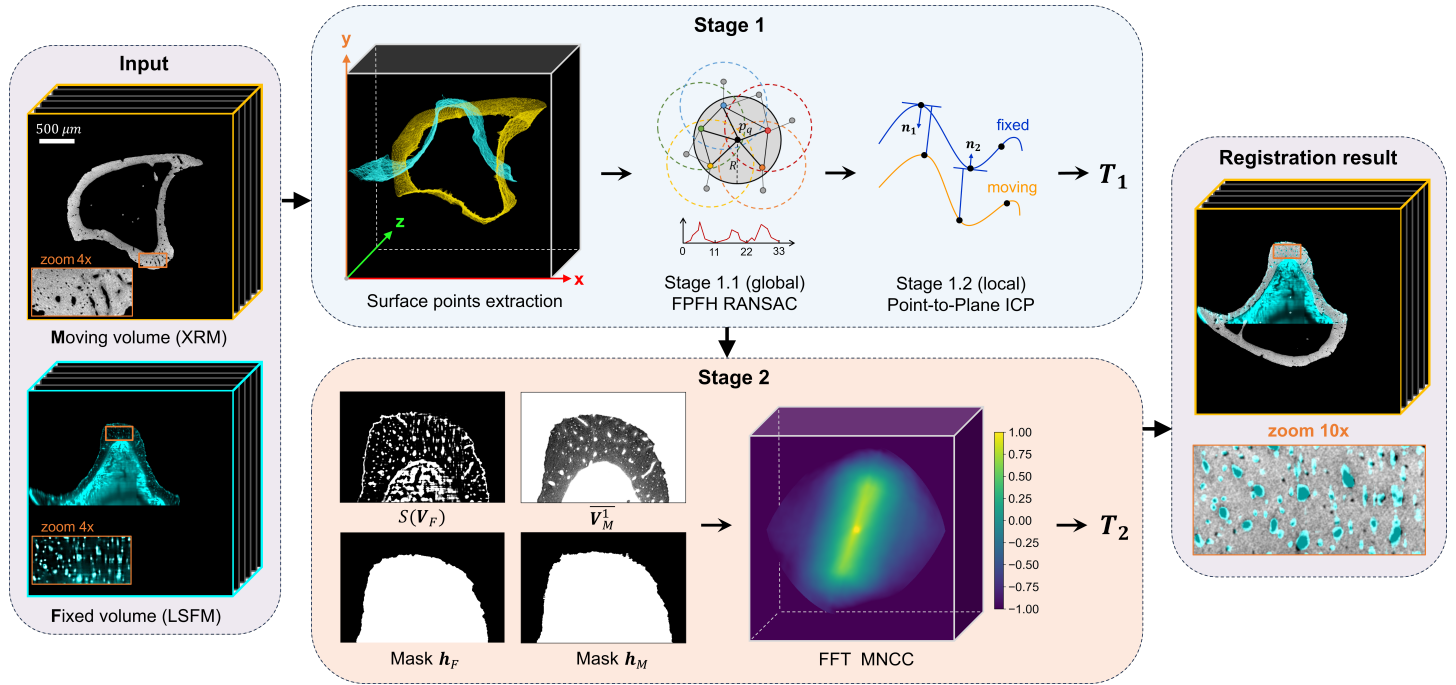


Figure 2: Illustration of BigReg pipeline. From left to right, the moving XRM volume needs to be rigidly transformed to align with the fixed LSFM volume. Stage 1 extracts surface features and performs two successive point cloud-based registration procedures to offer a coarse alignment  $\mathbf{T}_1$ . Stage 2 refines this alignment using masked normalized cross-correlation (MNCC) in the Fourier domain to achieve finer volumetric registration  $\mathbf{T}_2$ . Finally, the registration result is automatically obtained by combining these two transformations.

and Theoharis, 2020; Viergever et al., 2016; Bharati et al., 2022; Sengupta et al., 2022). Progress has been notable in modalities such as CT to magnetic resonance imaging (MRI) or within multi-channel MRIs. Focusing on 3D rigid transformation (3D rotation and translation), we categorize existing methods into three groups and discuss their challenges in managing the complex modalities addressed in this study.

## 2.1 Feature-based methods

Feature-based methods rely on extracting salient features common to different images, such as surface contours (Song et al., 2017; Sinko et al., 2018; Harada et al., 2008) and anatomical landmarks (Strasters et al., 1997; Pennec et al., 2000). As an easily available feature without the need for fiducial markers, surface-based approaches perform reliably by finding point-to-point correspondences using matching techniques like iterative closest points (ICP) (Besl and McKay, 1992; Yang et al., 2015). Registration using these geometrical features benefits from efficient processing time due to the reduced data amount. However, they restrict themselves to a subset of the available volumetric information which does not meet the fine-grained registration accuracy required by microstructure analysis (Savva et al., 2016).

## 2.2 Intensity-based methods

In contrast, intensity-based methods take full image contents into account and iteratively optimize transformation parameters to reach a maximum similarity measure between two images (Rahunathan et al., 2005; Avants et al., 2009; Modat et al., 2014; Klein et al., 2009). The choice of metrics depends on the modality differences, with mutual information (MI) (Rahunathan et al., 2005; Sengupta et al., 2022) commonly used across different modalities and cross-correlation (CC) (Avants et al., 2008) within the same modalities. Despite their popularity, these methods are infeasible for large-sized volumes with billions of voxels, as each iteration step executes an intermediate transformation interpolating the entire volume which is both computationally intensive and time-consuming. Moreover, issues like partial overlap and extreme misregistrations can lead to higher similarity scores for incorrect alignments, causing convergence failures of the non-convex function (Sengupta et al., 2022).

## 2.3 Learning-based methods

Recent deep learning-based (DL) methods (Bharati et al., 2022; Wang et al., 2023; De Vos et al., 2019; Lee et al., 2019) unsupervisedly register images using deep convolutional layers to extract 3D features, subsequently regressing transformation parameters through linear layers or a center-

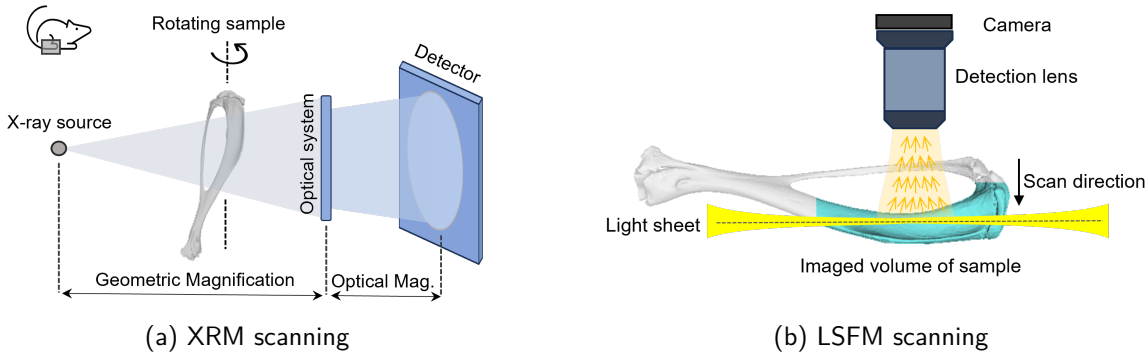


Figure 3: Illustration of scanning procedure of (a) XRM and (b) LSFM. Specifically, XRM captures high-resolution projection images through the two-stage magnification architecture; LSFM records horizontal slices illuminated by the corresponding thin light sheet.

of-mass layer (Ma et al., 2020). These methods utilize loss functions similar to those in classical approaches (Wang et al., 2023). Unfortunately, for clinical applications involving unique biological samples, the available data are often too sparse to support data-driven learning. Meanwhile, maintaining full resolution in 3D data is crucial as downscaling would dissolve critical tiny structures. Yet, the generic GPU memory is inadequate to handle such large datasets, further impeding the training of deep neural networks. Therefore, DL methods are not considered in this paper.

### 3. Methods

#### 3.1 Data description and preprocessing

XRM and LSFM utilize distinct imaging protocols, as illustrated in Fig. 3. In XRM scanning, X-ray beams pass through a rotating sample, which are subsequently converted into visible light via an optical system. A detector captures the attenuated photons to create 2D projections which are then used for 3D reconstruction. With different X-ray absorption rates, bone structures are imaged at higher intensity against soft tissues' markedly lower intensity, revealing blood vessel canals and lacunae. Conversely, LSFM is an optical imaging method relying on fluorescent markers. To highlight functional soft tissues within the bones, vessels, bone cells, and bone marrow are labeled with specific fluorescent stains, whereas bones are rendered transparent (Santi, 2011). During scanning, a light sheet illuminates a fluorescence plane, capturing one slice of the sample area with a camera. The scanner collects a series of slices by moving the light sheet along the scan direction, forming a 3D volume. Therefore, LSFM images capture fluorescing soft tissues with high intensity, offering a complementary view to those obtained by XRM.

Table 1 and Table 2 respectively summarize the key parameters of XRM and LSFM scan settings used in our

experiments, with the registration-related image attributes highlighted in bold. To standardize the data for registration, we undertake several preprocessing steps for each volume pair: Firstly, the LSFM volume is resliced and rescaled to match the XRM scan's coordinate system and resolution of  $1.42\text{ }\mu\text{m}$  in all dimensions; Secondly, the distal bone segments comprising 800 slices are selected to focus on medically most relevant regions; Finally, both volumes are zero-padded to achieve uniform dimensions of  $2048 \times 2048 \times 800$  and normalized to  $[0, 255]$ . Fig. 1 shows an example of the processed volume pair, with target microstructures labeled in the magnified subregions. Compared to the entire bone structure in the XRM reconstructed volume, the lower portion of the bone cross-section in the LSFM volume has not been acquired due to significant scattering artifacts. In the following registration process, we define XRM as the moving volume ( $V_M$ ) and LSFM as the fixed volume ( $V_F$ ).

#### 3.2 Stage 1: surface point cloud registration

The first stage of the registration pipeline starts with extracting surface point clouds from two volumes. We begin with segmenting the bone shape at a low threshold ( $V_M > 5$  and  $V_F > 0$ ). A series of binary morphological operations—comprising binary closing, hole filling, and outlining—is then performed on each slice to delineate the surface contours. The coordinates of all surface points are extracted to form point clouds. As illustrated in the upper middle part of Fig. 2, the moving point cloud  $P_M \in \mathbb{Z}^{3 \times N_M}$  is rendered in yellow, whereas the fixed point cloud  $P_F \in \mathbb{Z}^{3 \times N_F}$  appears in cyan, where  $N_M$  and  $N_F$  represent the number of points in  $P_M$  and  $P_F$ , respectively. After generating these two surface point clouds, we initially align their centers to minimize the initial displacement and prepare for the subsequent two substages of registration.

Device: Xradia 620 Versa microscope (Carl Zeiss)	
X-ray source voltage	60 kVp
X-ray source current	108 $\mu$ A
Number of projection images	1401
Angular range	202° (short scan)
Detector shape	2038 × 2038
Detector pixel size	11.0 $\mu$ m
Source-isocentre distance	16.5 mm
Isocentre-detector distance	16.0 mm
Magnification (geometrical/optical/total)	1.97/4/7.88
<b>Reconstructed volume shape</b>	1997 × 2038 × 2014
<b>(height × width × slices)</b>	
<b>Voxel size</b>	1.42 × 1.42 × 1.42 $\mu$ m <sup>3</sup>

Table 1: XRM scan settings

### 3.2.1 Stage 1.1: FPFH RANSAC

In substage 1.1, we employ the fast point feature histogram (FPFH) descriptor (Rusu et al., 2009) to map each point of  $\mathbf{P}_M$  and  $\mathbf{P}_F$  into a 33-dimensional feature vector, resulting in  $\mathbf{P}_M^{FPFH} \in \mathbb{R}^{33 \times N_M}$  and  $\mathbf{P}_F^{FPFH} \in \mathbb{R}^{33 \times N_F}$ . The FPFH feature captures the geometric relationship histogram between a source point and its specified number of neighbors within a defined spherical range (Rusu et al., 2009). Two hyperparameters are used to determine the search space:  $n_{FPFH}$ , the maximum number of neighbors, and  $r_{FPFH}$ , the radius of the sphere. Therefore, the corresponding point pairs can be found by querying the nearest neighbors in the global FPFH feature space. We apply the random sampling consensus (RANSAC) algorithm (Fischler and Bolles, 1981) to iteratively fit a rigid transformation model between the two point clouds, following these steps:

- Randomly pick three points from  $\mathbf{P}_M^{FPFH}$  and detect their corresponding points from  $\mathbf{P}_F^{FPFH}$  using nearest neighbor search in the FPFH feature space, facilitated by a K-D Tree (Bentley, 1975).
- For these matched point pairs, compute a hypothesized transformation matrix  $\mathbf{T} \in \mathbb{R}^{4 \times 4}$  based on Umeyama least-squares estimation (Umeyama, 1991).
- Apply  $\mathbf{T}$  to  $\mathbf{P}_M$  and determine the number of inliers, where inliers are considered as those neighboring point pairs from two point clouds with distances below a pre-defined threshold of  $d_{FPFH}$ .
- Repeat the above steps until the maximum number of iterations,  $iter_{FPFH}$ , is reached, and then return the

Device: Ultramicroscope II (Miltenyi Biotec)	
Illumination	Bidirectional
Number of light sheets	1
Light sheet width	20 mm
Zoom	Mono zoom
Zoom ratio	2.0
Objective lenses	2
Total magnification	4.0
Numerical aperture (NA)	0.5
NA for the sheet thickness	0.16
<b>Volume shape (height × width × slices)</b>	2048 × 2048 × 504
<b>Voxel size</b>	1.51 × 1.51 × 4.00 $\mu$ m <sup>3</sup>

Table 2: LSFM scan settings

transformation matrix with the highest number of inliers.

Since the correspondence detection is executed for all points, this substage is able to provide a global surface registration without prior alignment, yielding an initial transformation matrix  $\mathbf{T}_{1.1}$ .

### 3.2.2 Stage 1.2: point-to-plane ICP

The FPFH RANSAC algorithm provides a suboptimal solution for registration due to its reliance on random sampling. Following a widely recognized workflow in point cloud registration (Zhou et al., 2018; Rusu and Cousins, 2011), we integrate the point-to-plane ICP (Chen and Medioni, 1992) to achieve local refinement. Given a pre-alignment  $\mathbf{T}_{1.1}$ , this method presumes the closest points as correspondences and iteratively refines the registration to achieve the tightest fit, as detailed in the following steps:

- Apply the current transformation  $\mathbf{T}$  to  $\mathbf{P}_M$ , resulting in the transformed point cloud  $\mathbf{P}'_M$ .
- Identify the set of closest point pairs  $\mathcal{K}\{(\mathbf{p}'_M^{(i)}, \mathbf{p}_F^{(i)})\}$ ,  $i = 0, \dots, N_F - 1$  from  $\mathbf{P}'_M$  and  $\mathbf{P}_F$ , considering a maximum correspondence distance  $d_{ICP}$ .
- Update  $\mathbf{T}$  by minimizing the following objective function with the Gauss-Newton optimizer

$$\mathcal{L}(\mathbf{T}) = \sum_{(\mathbf{p}'_M^{(i)}, \mathbf{p}_F^{(i)}) \in \mathcal{K}} [\mathbf{n}^{(i)} \cdot (\mathbf{p}_F^{(i)} - \mathbf{T}\mathbf{p}'_M^{(i)})]^2, \quad (1)$$

where  $\mathbf{n}^{(i)}$  is the surface normal vector at point  $\mathbf{p}_F^{(i)}$ .

(iv) Repeat the steps until the designated maximum number of iterations ( $iter_{ICP}$ ) is reached and determine the final transformation.

At the end of this process, the refined transformation  $\mathbf{T}_{1.2}$  that accurately aligns the two point clouds is derived. The output of the first stage is updated as  $\mathbf{T}_1 = \mathbf{T}_{1.2}$  that transforms the moving volume to  $\mathbf{V}_M^1 = a(\mathbf{V}_M, \mathbf{T}_1)$ , where  $a(\cdot)$  represents the rigid transformation with bicubic interpolation.

### 3.3 Stage 2: volumetric registration

Following the surface registration, stage two aims to correct the residual misalignments of microstructures within the bone. Re-observing the image contents in Fig. 1, vessel canals and lacunae which manifest as tiny holes with nearly zero intensity in XRM volumes, contrast sharply with the bright, high-intensity representations of stained vessels and cells in LSFM volumes. These opposite intensity features can be matched by inverting the voxel intensity of XRM volume, yielding  $\overline{\mathbf{V}_M^1}$ . To eliminate the influence of the background outside the bone, binary bone masks  $\mathbf{h}_F$  and  $\mathbf{h}_M$  are generated for  $\mathbf{V}_F$  and  $\overline{\mathbf{V}_M^1}$  respectively using thresholding at zero followed by hole-filling operations. In addition, we apply the unsharp mask algorithm (Morishita et al., 1988) with a Gaussian kernel of 5 and weight of 0.8 for LSFM to reduce low-frequency scattering and enhance feature contrast, producing  $S(\mathbf{V}_F)$ . Four cropped slices from  $S(\mathbf{V}_F)$  with mask  $\mathbf{h}_F$  and  $\overline{\mathbf{V}_M^1}$  with mask  $\mathbf{h}_M$  are shown in the lower middle part of Fig. 2. For brevity, we redefine  $S(\mathbf{V}_F) \odot \mathbf{h}_F$  as  $\mathbf{V}_1$  and  $\overline{\mathbf{V}_M^1} \odot \mathbf{h}_M$  as  $\mathbf{V}_2$ , where  $\odot$  is element-wise multiplication.

Now, the high-intensity voxels in both  $\mathbf{V}_1$  and  $\mathbf{V}_2$  present the same semantic in bones. An optimal registration is achieved by finding a transformation  $\mathbf{T}_2$  that maximizes the sum of the product of  $\mathbf{V}_1$  and  $a(\mathbf{V}_2, \mathbf{T}_2)$ . Given that large displacement and rotation have been compensated during the surface registration phase, the remaining transformation can be approximated as a tight 3D translation, where  $\mathbf{T}_2 \approx [\Delta x, \Delta y, \Delta z]$ . We conduct an exhaustive search for  $\mathbf{T}_2$  using masked normalized cross-correlation (MNCC), formulated as

$$MNCC(\mathbf{T}_2) = \frac{\sum [(\mathbf{V}_1 - \mu_1)(a(\mathbf{V}_2, \mathbf{T}_2) - \mu_2)]}{\sqrt{\sum (\mathbf{V}_1 - \mu_1)^2} \sqrt{\sum (a(\mathbf{V}_2, \mathbf{T}_2) - \mu_2)^2}}, \quad (2)$$

where  $\mu_1$  and  $\mu_2$  represent the mean value of  $\mathbf{V}_1$  and  $a(\mathbf{V}_2, \mathbf{T}_2)$  within the overlapping regions of  $\mathbf{h}_F$  and  $a(\mathbf{h}_M, \mathbf{T}_2)$  respectively.

Like the cross-correlation in the spatial domain has its dual in the Fourier domain (Bracewell and Kahn, 1966), MNCC also benefits from a Fourier transform variant (Padfield, 2011), enabling efficient computation across all potential

transformations using the fast Fourier transform (FFT). This approach is vital for large volumes as it bypasses the need for direct transformations in the spatial domain, significantly accelerating the registration process. The outcome of the FFT MNCC operation generates a comprehensive search space of the same size as the original volume, as illustrated in the lower middle section of Fig. 2. Each coordinate represents a relative translation ( $[0, 0, 0]$  at the center), and the intensity corresponds to the MNCC score within the range of  $[-1, 1]$ . The optimal transformation is identified as the offset from the center to the location with the peak correlation score. Consequently, the overall transformation, combining both stages, is given as  $\mathbf{T}_{overall} = \mathbf{T}_2 \mathbf{T}_1$ .

## 4. Experimental setup

### 4.1 Data

We used a total of seven ex-vivo mouse tibial samples, each independently scanned by XRM and LSFM to create corresponding volume pairs. For the experiments, we augmented the dataset by applying a random pre-transformation to each registration run with rotations ranging from  $[-180^\circ, 180^\circ]$  and translations from  $[0, 100]$  on the xy-plane. To expedite processing, all intermediate transformations utilized linear interpolation. All experiments were conducted on identical hardware configurations, specifically an Intel i5-13500 CPU with 64 GB RAM.

### 4.2 Hyperparameters

The first stage of our pipeline depends on hyperparameters affecting the surface point cloud. We determined the most robust set of hyperparameters through extensive grid searching. For stage 1.1, the optimal parameters identified were:  $iter_{FPFH} = 2.5 \times 10^6$ ,  $r_{FPFH} = 200$ ,  $n_{FPFH} = 400$ , and  $d_{FPFH} = 30$ . For stage 1.2, the optimal hyperparameters were  $d_{ICP} = 16$  and  $iter_{ICP} = 2000$ .

### 4.3 Evaluation

To evaluate our method, we manually annotated 50 pairs of landmarks for each volume pair, focusing on corresponding anatomical microstructures under the supervision of biological experts. All landmark coordinates were distributed widely in 3D space, each at a distance of more than 100  $\mu\text{m}$  from its nearest neighbors. We employed RANSAC with  $10^5$  iterations and three correspondences to derive a transformation matrix for these defined landmark pairs. This landmark-based registration (LMR) serves as our ground truth (GT). In addition, four metrics are used for quantitative evaluation:

- **Landmark distance (LMD)** measures the average distance between moved XRM landmarks and fixed LSFM

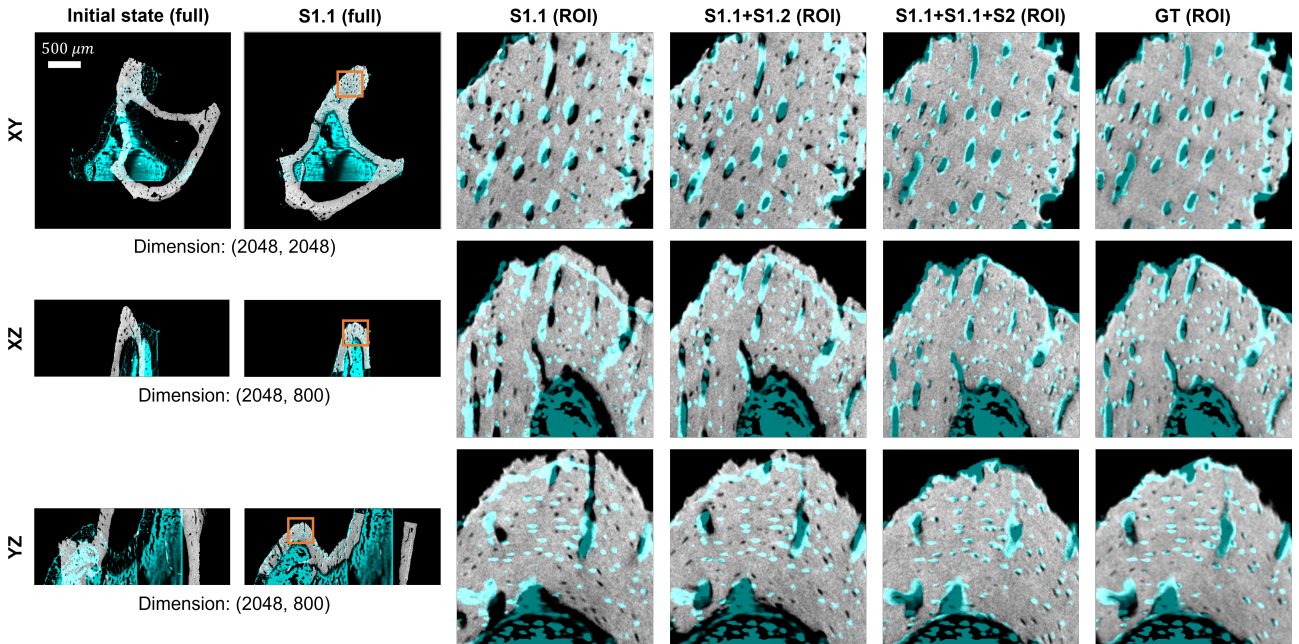


Figure 4: Visualization of the registration process in BigReg. Rows display central slices from different planes of the same sample. Columns one and two show the entire views at the initial state and S1.1, respectively, with specified dimensions. The subsequent three columns highlight eightfold magnified regions of interest (ROIs) from the  $256 \times 256$  orange boxes through successive registration stages. The last column displays the GT result.

BigReg Component	Only S1.1	Only S1.2	S1.1+S1.2	S1.1+S2	S1.1+S1.2+S2
LMD [ $\mu\text{m}$ ] ( $\downarrow$ )	$43.27 \pm 16.09$	$894.84 \pm 468.08$	$25.91 \pm 0.52$	$16.08 \pm 5.38$	$8.36 \pm 0.12$
LM fitness [%] ( $\uparrow$ )	$7.23 \pm 0.09$	$0.03 \pm 0.00$	$27.65 \pm 0.01$	$47.67 \pm 17.58$	$85.71 \pm 1.02$
Rotation error [ $^\circ$ ] ( $\downarrow$ )	$2.52 \pm 0.64$	$88.65 \pm 55.16$	$0.71 \pm 0.01$	$2.25 \pm 0.86$	$0.71 \pm 0.01$
Translation error [ $\mu\text{m}$ ] ( $\downarrow$ )	$73.06 \pm 20.88$	$2758.81 \pm 1535.46$	$40.11 \pm 0.76$	$65.12 \pm 31.26$	$13.90 \pm 0.35$

Table 3: Ablation study results for different pipeline configurations, reflecting mean and standard deviation across all samples when tested 100 times with random initial transformations.

landmarks.

- **Landmark fitness (LM fitness)** quantifies the inlier ratio of the landmarks, where the inlier threshold is set to  $12 \mu\text{m}$ .
- **Rotation error** refers to the minimum angular difference needed to align the estimated and GT rotation in space.
- **Translation error** is the Euclidean distance between the estimated and GT translation vectors.

## 5. Results

### 5.1 Ablation study

To assess the contribution of each component within the BigReg pipeline, we conducted an ablation study under various configurations: “only stage 1.1 (S1.1)”, “only stage 1.2 (S1.2)”, “S1.1+S1.2”, “S1.1+S2”, and the complete pipeline “S1.1+S1.2+S2”. Table 3 presents averaged results across all samples, each tested 100 times with random

initial transformations to gauge robustness. As evidenced in the second and third columns of the table, results from “only S1.1” are absolutely better than those from “only S1.2”. Adhering to a global-to-local registration strategy, S1.2 notably enhances the performance initiated by S1.1. From the fourth to the last column, we can observe that the full BigReg pipeline yields the highest performance across all metrics and demonstrates substantial robustness with the lowest standard deviation, whereas removing either S1.2 or S2 will degrade the performance. These findings are further visualized in Fig. 4, which illustrates the progressive alignment of target microstructures throughout successive stages of the BigReg process, culminating in precise alignment after the full pipeline execution.

### 5.2 Comparison against baselines

#### 5.2.1 Baselines

We compare BigReg against several baseline methods:

- **LMR:** As described earlier, LMR using 50 manually an-

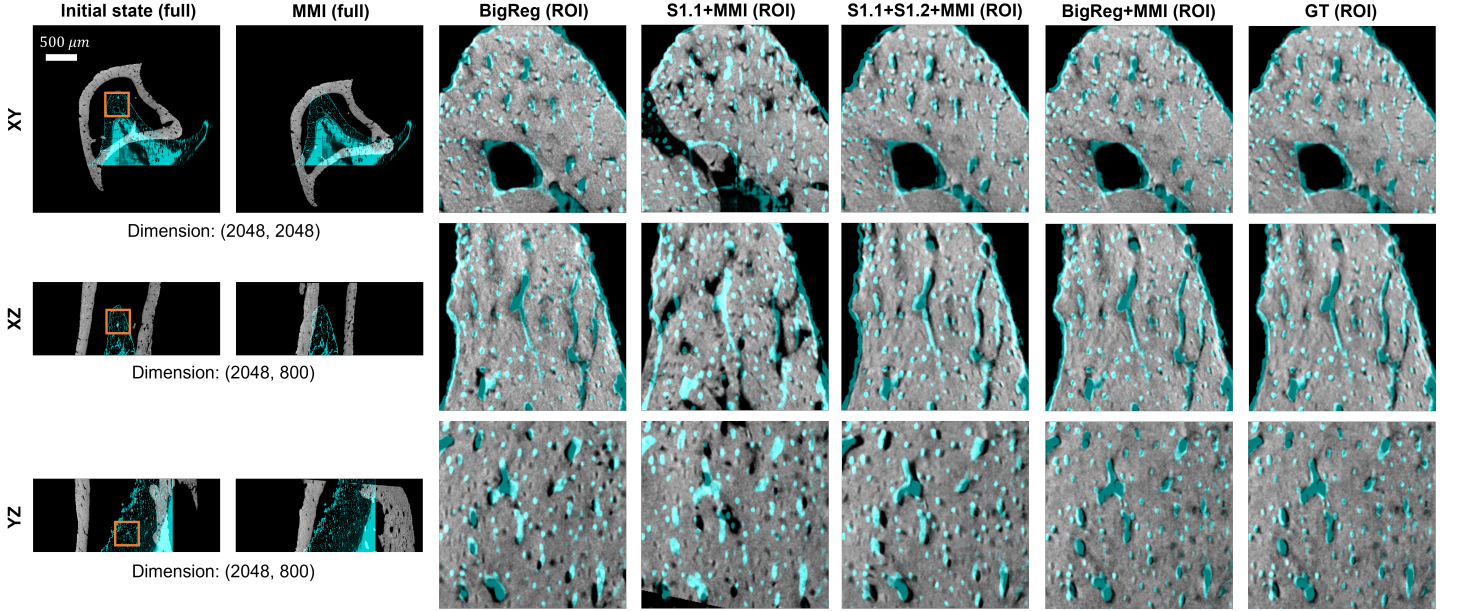


Figure 5: Qualitative results on an extremely misregistered example. Rows display central slices from different planes of the same sample. The first column shows the initial state in full view. Except for the second column which presents MMI's failed result, subsequent columns highlight eightfold magnified ROI from the  $256 \times 256$  orange boxes, corresponding to the applied methods.

Methods	MMI	BigReg	S1.1+MMI	S1.1+S1.2+MMI	BigReg+MMI
LMD [ $\mu\text{m}$ ] ( $\downarrow$ )	$>1000$	$8.36 \pm 0.12$	$19.12 \pm 20.54$	$8.50 \pm 5.46$	$7.24 \pm 0.11$
LM fitness [%] ( $\uparrow$ )	0.00	$85.71 \pm 1.02$	$83.14 \pm 20.78$	$93.78 \pm 4.11$	$93.90 \pm 0.77$
Rotation error [ $^\circ$ ] ( $\downarrow$ )	$>120$	$0.71 \pm 0.01$	$0.63 \pm 0.60$	$0.32 \pm 0.10$	$0.34 \pm 0.04$
Translation error [ $\mu\text{m}$ ] ( $\downarrow$ )	$>2000$	$13.90 \pm 0.35$	$29.26 \pm 34.32$	$10.63 \pm 5.02$	$11.29 \pm 1.44$

Table 4: Quantitative results compared with different baseline methods. The statistical mean and standard deviation were calculated by randomly transforming each sample 100 times. Note that an intrinsic LMD of  $6.10 \mu\text{m}$  exists in the GT result.

notated landmarks is treated as the ground truth (GT), although it has an average LMD of  $6.10 \mu\text{m}$  due to minor annotation and measurement errors.

- **Matthes mutual information (MMI):** MMI (Matthes et al., 2001) is a classical but most universal baseline. We utilize the implementation in ANTs, a state-of-the-art software framework for medical image registration (Avants et al., 2009). Specifically, we provide the bone masks to normalize the partial overlap and employ a multi-resolution pyramid strategy, registering volumes progressively at three different resolutions: 0.25x, 0.5x, and finally at full resolution.
- **Initializers+MMI:** We observe that MMI tends to be significantly affected by large initial misregistration. To investigate the effectiveness of MMI, we provide different-level initializations from BigReg to drive it. Here, we separately allocated "S1.1", "S1.1+S1.2", and the full BigReg as initializers to MMI. To the best of our knowledge, this idea has never been mentioned by other existing ap-

proaches. Therefore, it's also regarded as an extension of our proposed method.

### 5.2.2 Qualitative and quantitative results

Fig. 5 displays results on a challenging misregistration case. From column two, it is evident that MMI alone fails to adequately register the volume. In contrast, BigReg alone aligns the microstructures accurately, except for minor differences in the YZ plane compared to GT (visual difference can be observed between columns three and seven of Fig. 5). Subsequent results demonstrate that MMI's performance is highly sensitive to initialization. While MMI with either "S1.1" or "S1.1+S1.2" performs worse than standalone BigReg (columns four and five), combining the full BigReg with MMI achieves the best alignment, virtually indistinguishable from GT (column six).

The same observation is reflected in the quantitative results in Table 4. MMI deviates significantly from GT across all metrics. In contrast, our proposed BigReg demon-

strates robust results, approximating GT with an LMD of  $8.36\text{ }\mu\text{m} \pm 0.12\text{ }\mu\text{m}$  and an LM fitness of  $85.71\% \pm 1.02\%$ . In column five, it is noteworthy that “S1.1+S1.2+MMI” slightly outperforms standalone BigReg in the mean values except for LMD, but it exhibits lower robustness with consistently higher standard deviations. Finally, the extended BigReg with MMI continues to improve performance, achieving the lowest LMD of  $7.24\text{ }\mu\text{m} \pm 0.11\text{ }\mu\text{m}$  and the highest LM fitness of  $93.90\% \pm 0.77\%$ , along with minimal rotation and translation errors.

## 6. Discussion

The presented pipeline solves micrometer-level registration within two steps, with both conducted in an efficient way considering the enormous volume size. According to the ablative experiments, each stage plays an indispensable role within the pipeline. S1.1 lays the groundwork by providing a global transformation, while S1.2 and S2 further enhance performance and robustness. Specifically, omitting S2 leads to remaining translation errors (as shown in Table 3, column four), and the removal of S1.2 increases the instability of the method (Table 3, column five).

Furthermore, our observations reveal that the optimization process for MMI tends to terminate prematurely, often yielding inadequate transformation parameters. This issue is evident in the second column of Fig. 5, where the moving volume adjusts only minimally, primarily the distance between the centers of the two volumes. We attribute this to severe partial overlap and misalignment, which misleadingly elevate the MI value and cause the optimization gradients to incorrectly direct the registration process. However, with proper initialization, MMI regains its effectiveness. Thus, the integration of BigReg and MMI represents a synergistic approach, where BigReg provides optimal initialization and MMI addresses the rotation errors that BigReg’s second stage might overlook.

In addition, it is meaningful to mention that BigReg avoids optimizing for the entire volume, which allows for completing the task within approximately ten minutes—two minutes for the registration algorithm and eight minutes for one interpolated transformation. Although MMI does not fully account for the registration time due to its early stopping, one can still imagine that the multiple intermediate transformations could take a significant amount of time, measured in hours.

Looking ahead, we plan to explore the development of an auto-adaptive point cloud-based method to refine the parameter-dependent stage one, aiming to broaden the applicability of our approach. Although our current focus is on XRM and LSFM data, the fundamental principles of BigReg could potentially be generalized to other complex medical datasets.

## 7. Conclusion

We present an automatic two-stage registration pipeline, BigReg, tailored for high-resolution XRM and LSFM volumes. This innovative pipeline achieves performance comparable to manually annotated landmark-based registration methods. Through extensive experimentation, we demonstrated that while MMI-based methods typically struggle with such challenging data, they can be revitalized by integration with BigReg, thus forming an enhanced version of the pipeline. Most importantly, with the successful fusion of two image modalities, it is for the first time possible to conduct large-scale studies quantifying the proportion of lacunae that contain osteocytes as a potential new biomarker for bone remodeling diseases.

## Acknowledgments

This work was supported by the European Research Council (ERC Grant No. 810316). Sample preparation was conducted at University Hospital Erlangen, and data collection at Fraunhofer Institute for Ceramic Technologies and Systems (IKTS) and Institute for Nanotechnology and Correlative Microscopy (INAM).

## Ethical Standards

All animal experiments in this study were performed in accordance with German legal and regulatory guidelines and were approved by the local animal ethics committee of the Regierung von Mittelfranken (TS-12/2015). Moreover, the procedures conformed to the guidelines of the Federation of European Laboratory Animal Science Associations and the ARRIVE (Animal Research: Reporting of In Vivo Experiments) guidelines. Female C57BL/6JRj mice (14 weeks old) obtained from the University Hospital Erlangen were used in the research. All mice were anesthetized and subjected to bilateral ovariectomy or a sham operation. For tissue sample preparation, the mice were euthanized by CO<sub>2</sub>. Tibiae were relieved from muscle tissue and post-fixed in 4% PFA/PBS (pH 7.4) for 4 hours at 4–8°C with gentle shaking. Tissue fixation was followed by 100% ethanol dehydration.

## Conflicts of Interest

We declare we don’t have conflicts of interest.

## Data availability

The dataset is available from the corresponding author upon

reasonable request.

## References

MP Akhter and RR Recker. High resolution imaging in bone tissue research-review. *Bone*, 143:115620, 2021.

Brian B Avants, Charles L Epstein, Murray Grossman, and James C Gee. Symmetric diffeomorphic image registration with cross-correlation: evaluating automated labeling of elderly and neurodegenerative brain. *Medical image analysis*, 12(1):26–41, 2008.

Brian B Avants, Nick Tustison, Gang Song, et al. Advanced normalization tools (ants). *Insight j*, 2(365):1–35, 2009.

Jon Louis Bentley. Multidimensional binary search trees used for associative searching. *Communications of the ACM*, 18(9):509–517, 1975.

Paul J Besl and Neil D McKay. Method for registration of 3-d shapes. In *Sensor fusion IV: control paradigms and data structures*, volume 1611, pages 586–606. Spie, 1992.

Subrato Bharati, M Mondal, Prajyot Podder, and VB Prasath. Deep learning for medical image registration: A comprehensive review. *arXiv preprint arXiv:2204.11341*, 2022.

Ron Bracewell and Peter B Kahn. The fourier transform and its applications. *American Journal of Physics*, 34(8):712–712, 1966.

Pascal R Buerzli and Natalie A Sims. Quantifying the osteocyte network in the human skeleton. *Bone*, 75:144–150, 2015.

Yang Chen and Gérard Medioni. Object modelling by registration of multiple range images. *Image and vision computing*, 10(3):145–155, 1992.

Michael A Clynes, Nicholas C Harvey, Elizabeth M Curtis, Nicholas R Fuglie, Elaine M Dennison, and Cyrus Cooper. The epidemiology of osteoporosis. *British medical bulletin*, 133(1):105–117, 2020.

Bob D De Vos, Floris F Berendsen, Max A Viergever, Hesam Sokooti, Marius Staring, and Ivana Isgum. A deep learning framework for unsupervised affine and deformable image registration. *Medical image analysis*, 52:128–143, 2019.

Martin A Fischler and Robert C Bolles. Random sample consensus: a paradigm for model fitting with applications to image analysis and automated cartography. *Communications of the ACM*, 24(6):381–395, 1981.

Anika Grüneboom, Ibrahim Hawwari, Daniela Weidner, Stephan Culemann, Sylvia Müller, Sophie Henneberg, Alexandra Brenzel, Simon Merz, Lea Bornemann, Kristina Zec, et al. A network of trans-cortical capillaries as mainstay for blood circulation in long bones. *Nature metabolism*, 1(2):236–250, 2019.

Kouhei Harada, Hyoungseop Kim, Joo Kooi Tan, Seiji Ishikawa, and Akiyoshi Yamamoto. Optimal registration method based on icp algorithm from head ct and mr image sets. In *2008 International Conference on Control, Automation and Systems*, pages 1268–1271. IEEE, 2008.

Stefan Klein, Marius Staring, Keelin Murphy, Max A Viergever, and Josien PW Pluim. Elastix: a toolbox for intensity-based medical image registration. *IEEE transactions on medical imaging*, 29(1):196–205, 2009.

Max Langer and Francoise Peyrin. 3d x-ray ultra-microscopy of bone tissue. *Osteoporosis International*, 27:441–455, 2016.

Matthew CH Lee, Ozan Oktay, Andreas Schuh, Michiel Schaap, and Ben Glocker. Image-and-spatial transformer networks for structure-guided image registration. In *Medical Image Computing and Computer Assisted Intervention–MICCAI 2019: 22nd International Conference, Shenzhen, China, October 13–17, 2019, Proceedings, Part II 22*, pages 337–345. Springer, 2019.

Amanda B Longo, Phil L Salmon, and Wendy E Ward. Comparison of ex vivo and in vivo micro-computed tomography of rat tibia at different scanning settings. *Journal of Orthopaedic Research*, 35(8):1690–1698, 2017.

Tianyu Ma, Ajay Gupta, and Mert R Sabuncu. Volumetric landmark detection with a multi-scale shift equivariant neural network. In *2020 IEEE 17th International Symposium on Biomedical Imaging (ISBI)*, pages 981–985. IEEE, 2020.

David Mattes, David R Haynor, Hubert Vesselle, Thomas K Lewellyn, and William Eubank. Nonrigid multimodality image registration. In *Medical imaging 2001: image processing*, volume 4322, pages 1609–1620. Spie, 2001.

Marc Modat, David M Cash, Pankaj Daga, Gavin P Winston, John S Duncan, and Sébastien Ourselin. Global image registration using a symmetric block-matching approach. *Journal of medical imaging*, 1(2):024003–024003, 2014.

Koichi Morishita, Shimbu Yamagata, Tetsuo Okabe, Tetsuo Yokoyama, and Kazuhiko Hamatani. Unsharp masking for image enhancement, December 27 1988. US Patent 4,794,531.

Dirk Padfield. Masked object registration in the fourier domain. *IEEE Transactions on image processing*, 21(5):2706–2718, 2011.

Xavier Pennec, Nicholas Ayache, and Jean-Philippe Thirion. Landmark-based registration using features identified through differential geometry, 2000.

Françoise Peyrin, Pei Dong, Alexandra Pacureanu, and Max Langer. Micro-and nano-ct for the study of bone ultrastructure. *Current osteoporosis reports*, 12:465–474, 2014.

Liza J Raggatt and Nicola C Partridge. Cellular and molecular mechanisms of bone remodeling. *Journal of biological chemistry*, 285(33):25103–25108, 2010.

Smriti Rahunathan, Don Stredney, P Schmalbrock, and Bradley D Clymer. Image registration using rigid registration and maximization of mutual information. In *13th Annu. Med. Meets Virtual Reality Conf*, 2005.

Radu Bogdan Rusu and Steve Cousins. 3d is here: Point cloud library (pcl). In *2011 IEEE international conference on robotics and automation*, pages 1–4. IEEE, 2011.

Radu Bogdan Rusu, Nico Blodow, and Michael Beetz. Fast point feature histograms (FPFH) for 3D registration. In *2009 IEEE international conference on robotics and automation*, pages 3212–3217. IEEE, 2009.

Evdokia Saiti and Theoharis Theoharis. An application independent review of multimodal 3d registration methods. *Computers & Graphics*, 91:153–178, 2020.

Peter A Santi. Light sheet fluorescence microscopy: a review. *Journal of Histochemistry & Cytochemistry*, 59(2):129–138, 2011.

Antonis D Savva, Theodore L Economopoulos, and George K Matsopoulos. Geometry-based vs. intensity-based medical image registration: A comparative study on 3d ct data. *Computers in biology and medicine*, 69:120–133, 2016.

Debapriya Sengupta, Phalguni Gupta, and Arindam Biswas. A survey on mutual information based medical image registration algorithms. *Neurocomputing*, 486:174–188, 2022.

Martin Sinko, Patrik Kamencay, Robert Hudec, and Miroslav Benc. 3d registration of the point cloud data using icp algorithm in medical image analysis. In *2018 ELEKTRO*, pages 1–6. IEEE, 2018.

Zhiying Song, Huiyan Jiang, Qiyao Yang, Zhiguo Wang, and Guoxu Zhang. A registration method based on contour point cloud for 3d whole-body pet and ct images. *BioMed Research International*, 2017(1):5380742, 2017.

Karel C Strasters, John A Little, Johannes Buurman, Derek LG Hill, and David J Hawkes. Anatomical landmark image registration: validation and comparison. In *International Conference on Computer Vision, Virtual Reality, and Robotics in Medicine*, pages 161–170. Springer, 1997.

Jenny Thai, John-Paul Fuller-Jackson, and Jason J Ivanusic. Using tissue clearing and light sheet fluorescence microscopy for the three-dimensional analysis of sensory and sympathetic nerve endings that innervate bone and dental tissue of mice. *Journal of Comparative Neurology*, 532(1):e25582, 2024.

Mareike Thies, Fabian Wagner, Yixing Huang, Mingxuan Gu, Lasse Kling, Sabrina Pechmann, Oliver Aust, Anika Grüneboom, Georg Schett, Silke Christiansen, et al. Calibration by differentiation–self-supervised calibration for x-ray microscopy using a differentiable cone-beam reconstruction operator. *Journal of Microscopy*, 287(2):81–92, 2022.

Shinji Umeyama. Least-squares estimation of transformation parameters between two point patterns. *IEEE Transactions on Pattern Analysis & Machine Intelligence*, 13(04):376–380, 1991.

Max A Viergever, JB Antoine Maintz, Stefan Klein, Keelin Murphy, Marius Staring, and Josien PW Pluim. A survey of medical image registration—under review, 2016.

Alan Q Wang, M Yu Evan, Adrian V Dalca, and Mert R Sabuncu. A robust and interpretable deep learning framework for multi-modal registration via keypoints. *Medical Image Analysis*, 90:102962, 2023.

Chun-Lin Xiao, Lu-Lin Liu, Wen Tang, Wu-Yang Liu, Long-Yan Wu, and Kai Zhao. Reduction of the trans-cortical vessel was associated with bone loss, another underlying mechanism of osteoporosis. *Microvascular Research*, 152:104650, 2024.

P-L Xiao, A-Y Cui, C-J Hsu, R Peng, N Jiang, X-H Xu, Y-G Ma, D Liu, and H-D Lu. Global, regional prevalence, and risk factors of osteoporosis according to the world health organization diagnostic criteria: a systematic review and meta-analysis. *Osteoporosis International*, 33(10):2137–2153, 2022.

Zhencheng Xiong, Ping Yi, Jiali Lin, Shengfeng Qiu, Li Shu, and Chi Zhang. Evaluation of the efficacy of stem cell therapy in ovariectomized osteoporotic rats based on

micro-ct and dual-energy x-ray absorptiometry: A systematic review and meta-analysis. *Stem Cells International*, 2021(1):1439563, 2021.

Jiaolong Yang, Hongdong Li, Dylan Campbell, and Yunde Jia. Go-icp: A globally optimal solution to 3d icp point-set registration. *IEEE transactions on pattern analysis and machine intelligence*, 38(11):2241–2254, 2015.

Nasibeh Yousefzadeh, Khosrow Kashfi, Sajad Jeddi, and Asghar Ghasemi. Ovariectomized rat model of osteoporosis: a practical guide. *EXCLI journal*, 19:89, 2020.

Qian-Yi Zhou, Jaesik Park, and Vladlen Koltun. Open3d: A modern library for 3d data processing. *arXiv preprint arXiv:1801.09847*, 2018.